



HAL
open science

High conductivity PEDOT:PSS through laser micro-annealing: mechanisms and application

Joe Troughton, Nathalie Peillon, András Borbély, Jhonatan Rodriguez-Pereira, David Pavlinak, Jan M Macak, Thierry Djenizian, Marc Ramuz

► To cite this version:

Joe Troughton, Nathalie Peillon, András Borbély, Jhonatan Rodriguez-Pereira, David Pavlinak, et al.. High conductivity PEDOT:PSS through laser micro-annealing: mechanisms and application. *Journal of Materials Chemistry C*, 2022, 10 (43), pp.16592 à 16603. 10.1039/D2TC03812A . emse-04649600

HAL Id: emse-04649600

<https://hal-emse.ccsd.cnrs.fr/emse-04649600v1>

Submitted on 18 Nov 2024

HAL is a multi-disciplinary open access archive for the deposit and dissemination of scientific research documents, whether they are published or not. The documents may come from teaching and research institutions in France or abroad, or from public or private research centers.

L'archive ouverte pluridisciplinaire **HAL**, est destinée au dépôt et à la diffusion de documents scientifiques de niveau recherche, publiés ou non, émanant des établissements d'enseignement et de recherche français ou étrangers, des laboratoires publics ou privés.

Cite this: DOI: 00.0000/xxxxxxxxxx

High conductivity PEDOT:PSS through laser micro-annealing: Mechanisms and application[†]

Joe Troughton,^{a *} Nathalie Peillon,^b Andras Borbely,^b Jhonatan Rodriguez-Pereira,^{c, d} David Pavlinak,^d Jan M. Macak,^{c, d} Thierry Djenizian,^{a, e} and Marc Ramuz^{a ‡}

Received Date

Accepted Date

DOI: 00.0000/xxxxxxxxxx

Conductive polymers represent the next generation of soft, flexible electronics. Poly(3,4-ethylenedioxythiophene):poly(styrenesulfonate) (PEDOT:PSS) is among the most widely used of these, despite having a relatively low conductivity when deposited in the standard form with no additional chemical dopants. This is often mitigated through chemical doping, but this is associated with changes in processing easy, mechanical stability, or compatibility. This paper reports a laser micro-annealing process for PEDOT:PSS, including process optimisation, investigation of the underlying mechanism, and application in organic electronics. The laser micro-annealing increases the material conductivity from 1 S cm⁻¹ to around 360 S cm⁻¹ without any additive or post-deposition chemical treatments. This process is used, along with a laser ablation step, to fabricate organic electrochemical transistors (OECTs). These show comparable performance to material fabricated with common additives, while allowing rapid production of myriad devices. The additive and photolithography free processes enables simple fabrication of devices without the processing complications introduced by the use of additional chemicals. Following process optimisation, detailed study of the material properties suggests the dominant mechanism for this conductivity enhancement is the agglomeration of PEDOT cores within the film, facilitated by the moderate local heating action of the laser.

1 Introduction

Poly(3,4-ethylenedioxythiophene):poly(styrenesulfonate) (PEDOT:PSS) is arguably the most widespread conducting polymer used in organic electronics, forming an integral part of organic photovoltaics² and LEDs,³ and is the basis for a host of new and emerging bioelectronic and neuromorphic devices.^{4–13} Alongside excellent optical properties and mechanical flexibility, a major advantage of PEDOT:PSS is the ready commercial availability of aqueous suspensions of the material, making it particularly well suited to low cost solution processing. Deposited from such aqueous dispersions, the material forms

a granulated structure with PEDOT-rich cores surrounded by a PSS-rich shell,¹⁴ figure 1. However, in this state PEDOT:PSS has a relatively low conductivity (≈ 1 S cm⁻¹), making it unsuitable for many applications. This low conductivity can be significantly improved by the addition of a variety of additives such as ethylene glycol (EG),^{15–17} dimethyl sulfoxide,¹⁸ ionic liquids,^{19,20} salts,^{20,21} polar compounds,^{22,23} or oxide based catalysts²⁴. Alternatively, post deposition treatments with co-solvents^{1,16,25–27} or strong acids^{28–33} can be used. All of these approaches have drawbacks in terms of processability,³⁴ changes in electrical and/or mechanical characteristics,³⁵ or damage to substrates.³⁶ In addition, these treatments are global, affecting the entire film, with no ability to spatially confine the treatment conductivity.

A promising alternative has recently been reported in which laser based micro-annealing gives spatial control of the conductivity of PEDOT:PSS without additional chemical dopants.^{34,37,38} These reports conclude that the laser annealing fragments the PSS shell at the top surface, and enables local migration of the PEDOT cores, leaving aggregated PEDOT cores exposed at the surface, facilitating charge transport between these cores.^{34,38} However, the relative importance of these two actions remains unclear. This approach to controlling the conductivity eliminates many of

^a Mines Saint-Etienne, Center CMP, Department FEL, F - 13541 Gardanne France

^b Mines Saint-Etienne, Univ Lyon, CNRS, UMR 5307 LGF, Center SMS, F - 42023 Saint-Etienne France

^c Center of Materials and Nanotechnologies, Faculty of Chemical Technology, University of Pardubice, Nám. Cs. Legií 565, 53002 Pardubice, Czech Republic

^d Central European Institute of Technology, Brno University of Technology, Purkyňova 123, Brno, Czech Republic

^e Al-Farabi Kazakh National University, Center of Physical-Chemical Methods of Research and Analysis, Almaty, Tole bi str., 96A, Kazakhstan

* joseph.troughton@dunelm.org.uk

‡ ramuz@emse.fr

† Electronic Supplementary Information (ESI) available online. See DOI: 00.0000/00000000.

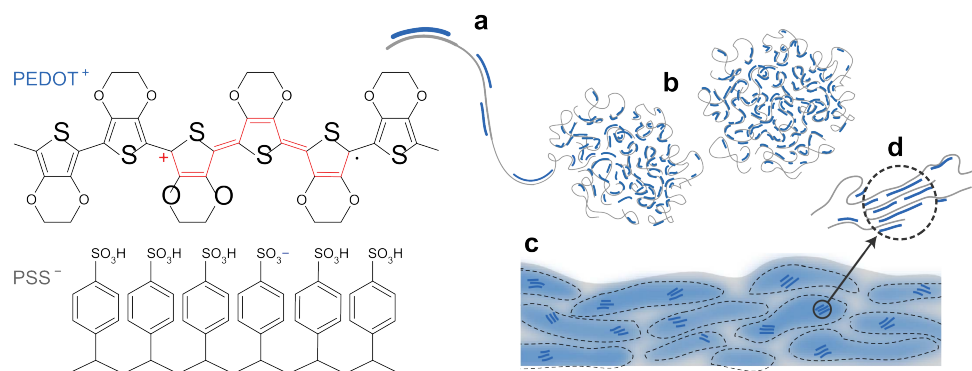


Fig. 1 PEDOT:PSS structure and morphology. The chemical structure of PEDOT:PSS and commonly described microstructure of the CP system a synthesis onto PSS template, b formation of colloidal gel particles in dispersion and c resulting film with PEDOT:PSS-rich (blue) and PSS-rich (grey) phases. d Aggregates/crystallites support enhanced electronic transport. Reprinted from¹ under CC BY 4.0 license.

the side effects of additives or post-deposition treatments while still allowing good control of the conductivity. However, owing to the immaturity of this process, a fully formed picture of the mechanisms underlying the change in conductivity is yet to form, and many potential applications remain unexplored.

This report first details the process of optimising the conductivity of PEDOT:PSS through laser micro-annealing. This is followed by a rigorous investigation of the material's electrical, morphological, and chemical characteristics, and discussion of these in terms of potential mechanisms underlying the process. Finally, laser micro-annealing is combined with the more established technique of PEDOT:PSS complete laser ablation to fabricate planar organic electrochemical transistors (OECTs)³⁹ in a simple, photolithography-free process, demonstrating behaviour on par with devices based on PEDOT:PSS with standard additives.

2 Laser Optimisation

Laser micro-annealing was performed on spin coated PEDOT:PSS using a pulsed 1064 nm Nd:YAG laser in a laser writing system (LPKF ProtoLaser S). After optimisation of the processing parameters, the sheet conductivity could be controlled from $1.1 \pm 0.1 \text{ S cm}^{-1}$ up to $360 \pm 11 \text{ S cm}^{-1}$. This is compared with PEDOT:PSS with a commonly used additive mixture which shows a conductivity of $343 \pm 13 \text{ S cm}^{-1}$ as prepared here. Multiple parameters can be controlled in the laser system, affecting both spatial uniformity and total power of the laser treatment. It should be noted that, while the process described here utilised a 1064 nm Nd:YAG laser system, as was used by Yun et al., the work of Ding et al. was based on a 10 600 nm CO₂ laser. It is expected that the optimisation process below, and the underlying materials changes, would be universal for most wavelengths, with optimal values dependent on laser power density and film absorption at the laser wavelength.

2.1 Focal Height

The laser used has a beam waist at focus of $25 \mu\text{m}$, see figure S1 of the electronic supplementary information (ESI)[†]. However, due to small changes in the power output of the laser system (predominantly due to temperature fluctuation, focal drift, and

possible multimodal laser characteristics) and the relatively low powers required, it was found that achieving consistent laser irradiation at the beam waist was a significant challenge. In order to eliminate the effect of these fluctuations, samples were offset from the focal point, at a point with a larger beam diameter, where fluctuations in height or power are minimised due to the beam spreading.

The sheet resistance of the PEDOT:PSS with irradiation at different focal heights can be seen in figure 2a. In figure 2a, a laser power of 4.2 W, line writing speed of 200 mm/s, and line separation of $200 \mu\text{m}$ were used. From figure S1[†] it can be seen that the measured spot size becomes nearly constant above a focal height of 10 mm (8 mm away from the beam waist) with a diameter of around $400 \mu\text{m}$, due to the small relative difference in power density at each step. This is reflected in figure 2a, where there is no further change in the sheet resistance at focal heights greater than 10 mm. In order to ensure that samples always remain within this parallel beam regime, even with small variations in sample thickness, a focal height of 11.5 mm was used for the remaining work unless otherwise indicated.

2.2 Line Spacing

The line spacing refers to the distance between the laser raster lines. The sheet resistance for increasing line spacing, measured parallel and perpendicular to the laser raster direction, can be seen in figure 2b, (measured in the van der Pauw setup shown in the inset). Above $300 \mu\text{m}$ there is a clear anisotropy in the sheet resistance. This is explained by the beam diameter ($400 \mu\text{m}$): at line spacings below $400 \mu\text{m}$ there is overlap of the beam between adjacent lines leading to (pseudo-)continuous irradiation of the film, while at greater separations, regions of unirradiated material exist between the parallel lines leading to anisotropic resistances. The optical images of figure S2[†] of the ESI clearly show this. Between $300 \mu\text{m}$ and $400 \mu\text{m}$, continuous irradiation across the film is achieved, but this does not remove the anisotropic resistance of the film. The Gaussian nature of the laser intensity explain this effect, as the edges of the laser beam do not provide sufficient power to affect the conductivity, leading to the presence of the anisotropy at spacing smaller than the beam

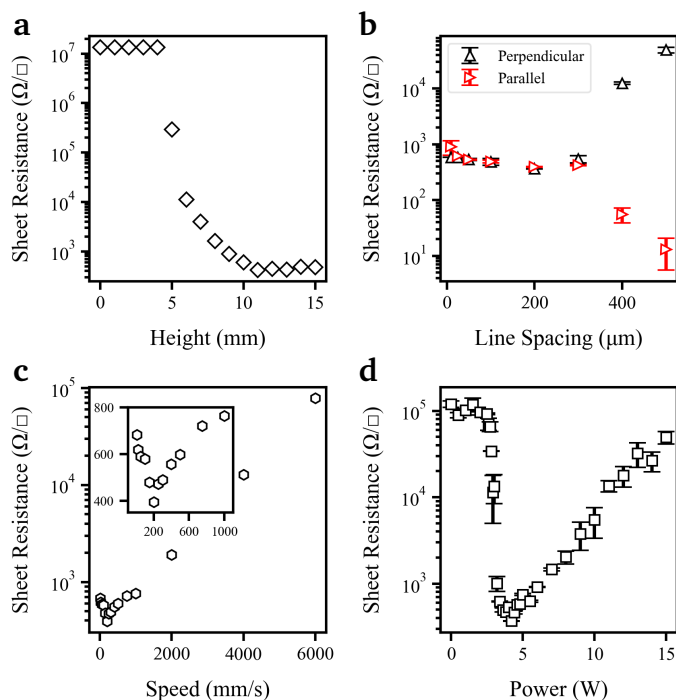


Fig. 2 Evolution of PEDOT:PSS sheet resistance with varying laser parameters: a focal offset height; b line spacing (measured parallel, red, and perpendicular, black, to the line writing direction, depicted in the inset schematic); c laser rastering speed, inset is a magnification of the data up to 1000 mm/s; d Laser power.

width. This is supported by the lowest observed sheet resistance occurring at 200 μm spacing, or spacing equal to half of the beam diameter. In this case, the entire film receives uniform irradiation, as described elsewhere.³⁷ 200 μm is, therefore, the spacing used for the remainder of this work.

2.3 Raster Speed

The speed of the laser rastering is another aspect that determines the homogeneity of the irradiation, due to the pulsed nature of the laser. In this work, a laser pulse frequency of 15 kHz was used. This rate is set in the control software, and confirmed by measuring the spacing of adjacent laser spots at different speeds (figure S3 of the ESI[†]). Figure 2c shows the sheet resistance of PEDOT:PSS irradiated with varying raster speeds. It was found that a minimum sheet resistance is achieved a raster speed of 200 mm/s. Above this the sheet resistance rises rapidly as the laser strike positions gets further apart. As with the anisotropy discussed above, this is caused by areas of unirradiated material occurring between the areas where the laser strikes. Below 200 mm/s the sheet resistance again rises, likely due to over exposure of the material. Hence, 200 mm/s is taken as the optimal raster speed, and used in the rest of this work.

2.4 Laser Power

While the optimisation of the previous parameters pertained primarily to the homogeneity of the irradiation across the film, the final parameter, the laser power, affects the conductivity that can be reached. Figure 2d shows the evolution of the sheet

resistance with increasing laser power using the optimised values from the previous sections. Here it is seen that low power irradiation, below 2.5 W (equivalent to a power density of around 20 W/mm^2), has little effect on the sheet resistance, consistent with previous reports.^{37,38} Above 2.5 W the sheet resistance drops rapidly to a minimum of $369 \pm 2 \Omega/\square$ at 4.2 W, followed by a gradual increase in sheet resistance as the laser power increases and the film is over irradiated. The correlation between the laser power and materials properties are discussed in the next section.

3 Characterisation of irradiated films

When first reported in 2019 by Yun et al., it was suggested that the primary mechanism responsible for conductivity change is the disruption of the PSS shells surrounding the PEDOT cores at the surface of the material.³⁴ However, Ding et al. proposed an alternative mechanism, wherein the laser treatment allowed aggregation of the PEDOT cores,³⁸ based on similar XPS data. Here, multiple routes are used to examine these mechanisms, along with other potential materials changes, the results of which are summarised in figure 3. These measurements are first described individually, followed by a holistic consideration of their implications in section 3.11.

3.1 PEDOT:PSS thickness and surface roughness

The first measures of the impact of laser treatment are the film thickness and roughness. Figure 3a shows the thickness of the PEDOT:PSS films after laser treatment. At low powers, below the threshold power of 2W, the film thickness remains constant, with a small degree of film swelling seen between 2 W and 3 W, and a gradual thinning of the film at higher powers. This indicates that above the optimum power, of 4.2 W ablation is removing material, thereby increasing the resistance. The film swelling may be due to the onset of PEDOT core movement before any ablation starts.

Alongside the swelling, optical profilometry measurements show the onset of waviness in the film perpendicular to the laser writing direction, seen in figure S4[†]. This waviness increases up to 5 W laser power, while the global film roughness also increases between 4 W and 5 W. Above 5 W, both the waviness and the roughness reduce as the film thickness reduces. This roughness change is exemplified by SEM images of figures 3k and 3l.

This increased roughness, and changing film thickness, are in direct contradiction to the reports of Yun and Ding,^{34,38} neither report investigate thickness or roughness changes in detail. Yun reported SEM cross sections before and after laser treatment, where no change in thickness was observed, along with SEM surface images showing little change in surface structure, although no roughness measurements were reported. Ding didn't report any change in film thickness with laser treatment, but did report a small increase in surface roughness above the optimal laser power, of just $2.50 \pm 0.138 \text{ nm}$ as measured by AFM. However, it is not reported over what area the AFM measurement was taken, making comparison to the work here challenging. The exact relationship between thickness changes, increases in roughness, and the introduction of waviness is somewhat

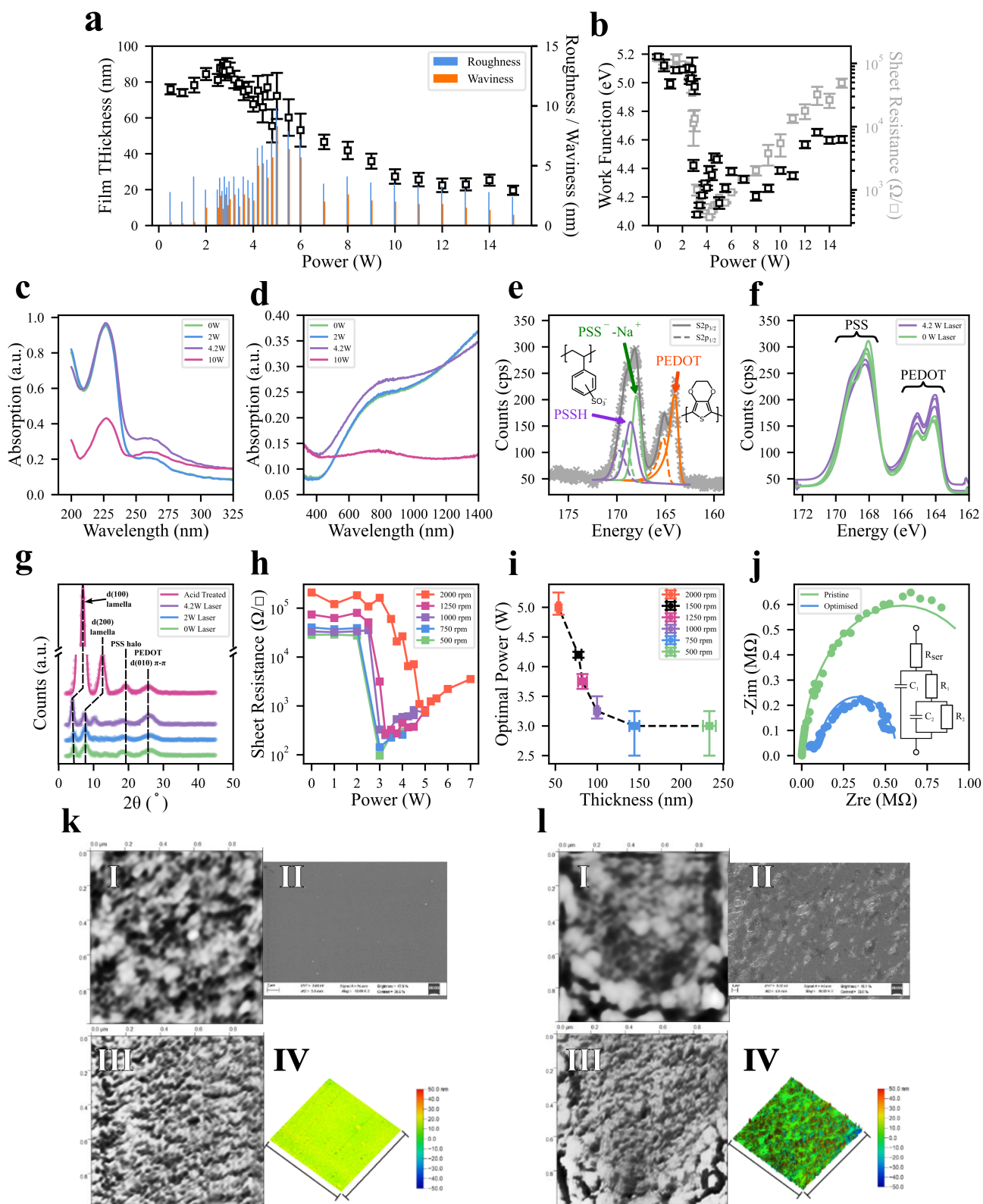


Fig. 3 Results of characterisation measurements. Caption on the next page.

Fig. 3 a Thickness, surface roughness, and waviness of PEDOT:PSS with increasing laser power. Error bars on the thickness are the arithmetic sum of the surface roughness and waviness. These data are included in table S1 of the ESI. b Work function of the PEDOT:PSS surface with increasing laser power. The sheet resistance for each sample is greyed out behind. c-d UV-vis absorption spectra for PEDOT:PSS films with different laser powers. in the ranges a 180 - 350 nm and b 380 - 1400 nm, separated to show the components on different scales. e S 2p XPS data for a single laser-treated PEDOT:PSS sample. Original data is shown by the grey crosses, the combined fitting function by the grey line, and the deconvolved peaks used to fit the data by the coloured lines. PEDOT peaks are shown in orange, PSS⁻-Na⁺ in green, and PSSH in purple. Each peak is split into spin-orbit 1/2 (dashed) and spin-orbit 3/2 (solid) components. f Fitted S 2p XPS envelopes for 3 laser-treated and 3 untreated samples. The PEDOT peaks are more prominent after laser treatment. g XRD patterns for PEDOT:PSS treated with different laser powers, and with concentrated H₂SO₄, after removal of a convex hull background. h Sheet resistance of PEDOT:PSS films with increasing laser power for films prepared at varying spin coating speeds. i Power at which the lowest sheet resistance was reached for films prepared at different spin coating speeds. j Electrochemical impedance spectra for laser-treated and untreated PEDOT:PSS files, fitted using the equivalent circuit shown. k AFM and SEM images for untreated PEDOT:PSS. I 1×1 μm AFM topography image of untreated PEDOT:PSS. II 15×11 μm SEM image of untreated PEDOT:PSS. III 1×1 μm AFM phase image of untreated PEDOT:PSS. IV 5×5 μm AFM topography projection of untreated PEDOT:PSS. | AFM and SEM images for laser-treated PEDOT:PSS. I 1×1 μm AFM topography image of laser-treated PEDOT:PSS. II 15×11 μm SEM image of laser-treated PEDOT:PSS. III 1×1 μm AFM phase image of laser-treated PEDOT:PSS. IV 5×5 μm AFM topography projection of laser-treated PEDOT:PSS.

uncertain. However, it can be supposed that the swelling of the film may be due to internal movement of the PEDOT cores, while the fall in thickness and increased roughness are due to the onset of material ablation.

These thickness changes may be thought to have implications for the material's conductivity dependence on treatment power. An estimate of this conductivity is shown in figure S5[†], where it can be seen that the general trend in film conductivity mirrors that of the sheet resistance of figure 2D.

3.2 Work Function

Another measure of the PEDOT:PSS surface is the work function. This can be seen for the laser-treated films in figure 3b. As with other measures, material treated with laser powers below the threshold show little change in work function from the pristine value of 5.19 eV, while a large drop is seen above the threshold, reducing to 4.1 eV, correlated strongly with the drop in sheet resistance. This supports the idea that PEDOT is more exposed at the surface after laser treatment as PSS shells generally increase the work function.^{34,40,41}

3.3 UV-Vis Spectroscopy

UV-Vis absorption spectra for a selection of laser powers can be seen in figure 3c & d. PSS is known to show two distinct absorption peaks below 250 nm, with the peak at around 230 nm shown in figure 3c.^{42,43} As the peak neither moves nor reduces in height after laser treatment, the total amount of PSS in the film remains constant up to at least the optimised laser power, suggesting that the removal of PSS is not the cause of the increased conductivity. This is in agreement with the works of Yun and Ding^{34,38} and in stark contrast to the behaviour seen when conductivity in controlled post deposition chemical treatments which remove excess PSS.⁴⁴ It is notable, however, that treatment with high power, above the optimum, does reduce the PSS peak as material is ablated and the film thins.

Figure 3d shows the absorption at longer wavelengths, into the near IR region. Absorption in this region is dominated by three bands, and their relative intensities are indicative of the oxidation state of the PEDOT,⁴⁵⁻⁴⁷ although the exact attribution of each band to polaron (+e) and bipolaron (+2e) states is disputed.⁴⁸

Nonetheless, it is understood that a decrease in absorption above 1100 nm, and an increase in absorption between 700 nm and 1100 nm, is indicative of a lowering of the oxidation state, with the eventual emergence of a further absorption band at around 600 nm as the material becomes fully reduced.⁴⁹ In our study, the laser treatment has no effect on absorption below the 2.5 W threshold, but above the threshold there is increased absorption in the 700 - 1100 nm range, and reduced absorption above 1100 nm. This suggests the PEDOT becomes somewhat reduced by the laser treatment. This is particularly surprising as reduction of the film is associated with reduced conductivity, not enhanced.⁵⁰

3.4 X-ray photoelectron spectroscopy

Having established that the total PSS content of the films is unchanged up to 4.2 W laser power, X-ray photoelectron spectroscopy (XPS) was used to assess the change in the PEDOT:PSS ratio at the surface. Figure 3e shows an example S 2p signal for PEDOT:PSS irradiated with 4.2 W laser power, along with the components used to fit the data. There are two distinct peaks, at around 168 eV and 164 eV, corresponding to the different binding energies of sulphur atoms in the PSS and PEDOT, respectively. The PEDOT peak is made up of a doublet centred at 164.0 eV / 165.2 eV, ascribed to the S 2p_{3/2} / S 2p_{1/2} spin-orbit splitting. The broad PSS peak is split into 4 components comprising the S 2p_{3/2} / S 2p_{1/2} of sulphur atoms in the PSS⁻-Na⁺ and PSSH forms, centred at 168.0 eV and 169.2 eV (PSS⁻-Na⁺) and 168.6 eV and 169.8 eV (PSSH).⁵¹ In figure 3f, the fitting outcome for three unirradiated and three 4.2 W laser-treated samples are shown. The PEDOT peak is significantly more prominent after laser treatment, indicating a larger proportion of PEDOT is exposed at the surface. These changes are summarised in table 1 and shown in detail in table S2 of the supplementary information.

3.5 X-Ray Diffraction

To assess any impact on crystallinity, X-ray diffraction (XRD) measurements were performed, figure 3g. In acid based treatments in particular, crystallisation is a significant contributor to the increased conductivity of the material. For comparison,

Table 1 Average results of fitting S 2p XPS data for laser-treated and untreated PEDOT:PSS. Values are given as percentage of the total sulphur content in each form, based on the area of the peaks fitted for each component. For full elemental analysis see table S2.

	Sulphur Atomic Concentration (%)			Ratio
	PEDOT (S ²⁻)	PSS-Na ⁺	PSSH	PEDOT/PSS
Untreated	35.7±0.4	38.4±5.1	25.9±5.2	0.56±0.01
Laser Treated	40.3±1.7	36.5±4.4	23.2±5.3	0.68±0.05

XRD data for PEDOT:PSS treated with concentrated H₂SO₄ are presented alongside laser irradiated material.

Figure 3g shows that the untreated films contain only a small amount of crystalline structure, with four peaks at around $2\theta=4.4^\circ$, 7.8° , 18.5° , and 26.2° . These peaks, while small, are characteristic of PEDOT:PSS. The first two peaks, with d spacings of 20.0 Å and 11.3 Å ($2\theta=4.4^\circ$ and 7.8°), are ascribed to the $d(100)$ and $d(200)$ lamella stacking of the PEDOT on PSS chains.⁵² The peak corresponding to the d spacing of 4.7 Å ($2\theta=18.5^\circ$) is associated with the amorphous PSS halo, while the one with d spacing of 3.4 Å ($2\theta=26.2^\circ$) is due to the $d(010)$ π - π stacking of the PEDOT.^{35,53}

These peaks become significantly more distinct after treatment with H₂SO₄, and there is a marked shift in the position of the two lamella stacking peaks corresponding to a 6.4 Å reduction in stacking distance, a well known effect of such acid treatment due to the removal of PSS.⁵⁴

In contrast, the laser treatment has a much weaker effect on the crystal structure of the films. At 2 W, the laser has no measurable effect, which agrees with other measurements in this work. At 4.2 W there are some small, but significant changes. First, the low angle peak, corresponding to the $d(100)$ lamella stacking in the PEDOT rich cores is enhanced, indicative of a larger crystallite size producing this reflection, here due to increased PEDOT core size. Second, this same peak shows a small shift to a lower angle, which can be described as an approximately 2 Å increase in the stacking distance. In addition, the $d(010)$ π - π stacking peak at $2\theta=26.2^\circ$ is somewhat enhanced, while remaining in the same position, further supporting the increased PEDOT domain size. Finally, there is an additional peak introduced at around $2\theta=10.3^\circ$, corresponding to the PSS to PSS lamella stacking distance of 8.6 Å.^{54,55}

3.6 AFM and SEM Imaging

Physical changes at the surface of the material can be examined through AFM and SEM imaging. AFM topography and phase images for 1×1 µm squares of pristine and laser-treated material can be seen in figures 3k and 3l, along with topological projections across 5×5 µm squares for the same materials, and 15×11 µm SEM images. Further comparison of SEM images can be found in the ESI, figure S6[†]. From both the 5 µm AFM images, and the SEM images, it is clear that there is considerable disruption to the film surface after laser treatment, corresponding to the increased film roughness discussed above. At the same time, the 1 µm AFM images clearly show a change in the morphology of the film, most clearly seen in the phase

images, which show a phase separation of the PEDOT and PSS and corresponding increases in PEDOT core sizes.^{45,50}

3.7 Film Drying

It is suggested by Ding et al.³⁸ that, in addition to fragmentation of surface PSS shells and movement of the PSS cores, the laser treatment also acts to locally dry the PEDOT:PSS, thereby increasing conductivity. To investigate this, additional films were prepared in a high and low hydration states by drying for 10 minutes at 100°C and for 30 minutes at 200°C, respectively. It was found that the as-deposited sheet resistance of high hydration films, 95 ± 10 kΩ/□, was in line with that of the standard process (15 minute drying at 120°C), at 100 ± 10 kΩ/□, whereas lower hydration films had a significantly lower sheet resistance of 50 ± 10 kΩ/□. However, while the resistance of the high hydration films fell to 400 ± 30 Ω/□ after optimal laser treatment, matching the values seen with the standard material, 369 ± 2 Ω/□, the low hydration material remains significantly more resistive, at 1.1 ± 0.1 kΩ/□. These data can be seen in figure S7[†]. These measurements suggest that in low hydration films, the position of the PEDOT cores is more firmly fixed such that they are unable to agglomerate during laser treatment, and so high conductivity cannot be reached. This, in turn, suggests that the agglomeration of the PEDOT cores is a significant factor in the changing conductivity observed.

3.8 Effect of Film Thickness

To further examine whether the effect of the laser treatment is seen throughout the film, or only at the surface, PEDOT:PSS films of varying thickness where examined. Films were prepared with spin coating speeds between 500 rpm and 2000 rpm, giving progressively thinner films. The results of laser powers between 0 W and 6 W can be seen in figure 3h.

If the effect of the laser treatment was confined to the top surface it may be expected that the optimal laser power would remain constant for all film thicknesses. However, as seen in figure 3i, there is a steady increase in the optimum power as the spin coating speed increases (so the film thickness decreases). This strongly suggests that the effect of the laser treatment is seen throughout the film, not only at the surface.

Indeed, the reduced optimal power with increasing thickness is direct evidence that the process occurs throughout the film, since an increasing film thickness is directly correlated with an increasing absorption of the incident laser light. This increasing absorption, in turn, leads to a greater heating effect in the film for the same power, shifting the optimal value lower. While it may be argued that the increasing thickness also means there is more mass of PEDOT:PSS to heat up, this is likely to be insignificant in comparison to the thermal mass of the glass substrate. Therefore, an increasing thickness leads to more heating at lower laser powers, reducing the optimal power needed to achieve the same heating effect.

3.9 Electrochemical Impedance

Figure 3j shows Nyquist impedance spectroscopy plots for PEDOT:PSS films with and without optimal laser treatment. These data were well fitted by a standard resistor/capacitor equivalent circuit for a strongly absorbing double layer,⁵⁶ as described by C. Grahame⁵⁷ (inset in figure 3j). Fitting for individual devices can be found in figure S9[†]. Fitting of these data showed that, as expected, the resistance of the laser-treated material is significantly lower than the untreated material. Specifically the series resistance (R_{ser}) fell from 33 ± 1 k Ω to just 1.0 ± 0.1 k Ω after laser treatment. Alongside the fall in resistance, the impedance spectroscopy also revealed a significant rise in the material's double layer capacitance, C_1 , as well as an increase in the level of absorbed ions, associated with C_2 after laser treatment.⁵⁸ There is also an increase in R_1 , the charge transfer resistance in this model, after laser treatment, while R_2 , which is associated with the activation energy of absorption/desorption, remains the same.

Table 2 Summarised results of impedance spectroscopy fitting with the equivalent circuit show in figure 3j.

	R_{ser} (k Ω)	R_1 (M Ω)	C_1 (pF)	R_2 (M Ω)	C_2 (nF)
Untreated	33 ± 1	0.10 ± 0.02	24 ± 4	0.5 ± 0.1	0.35 ± 0.05
Laser-Treated	1.0 ± 0.1	1.1 ± 0.5	355 ± 43	0.5 ± 0.5	2 ± 1

3.10 Thermal modelling of laser interaction

Previous works have indicated the likely mechanism for the laser-mediated conductivity changes is thermal. In particular, it is suggested that the absorption of the laser energy by the PEDOT cores leads to local heating in the film. In order to understand the extent of this laser heating, finite element analysis (FEA) was employed to study the local and global heating effect of the laser, using COMSOL Multiphysics. At the optimal laser power of 4.2 W, it was found that each laser pulse caused a local temperature spike of around 50°C. This was confined in the in-plane dimensions to a full width at half maximum (FWHM) around 200 μm diameter perpendicular to the direction of travel of the laser and around 450 μm in the direction of travel, owing to the accumulation of heat from the laser. The rise in temperature takes around 1 ms to reach the maximum before the temperature follows an exponential decay back to the ambient temperature with a half-life of 1.3 ms, figure S8[†]. It was also found that the time between laser pulses, along with the spatial offset of each pulse strike, was sufficient to allow the film to cool back to the ambient temperature, meaning there was no overall increase in temperature in the film with time.

Figure S8b[†] shows the monotonically increasing peak temperature induced by the laser at increasing powers. It can be inferred from the physical measurements that this increasing temperature corresponds to increasing ablation of the PEDOT:PSS.

3.11 Interpretation of results

Throughout these measurements it is shown that laser treatment leads to both morphological and chemical changes in the PEDOT:PSS films, but that these changes have a threshold laser fluence needed before they start to take effect. Above this threshold, an optimal power is quickly reached, followed by a slower decline in conductivity. This later effect can be attributed to the onset of material ablation, causing a significant increase in film roughness as well as an overall thinning as the power increases above the optimum.

The transition from unaffected to peak conductivity films, however, is more subtle. The XPS results, figure 3f and table 1, clearly show increased PEDOT at the surface after the laser treatment. This is aligned with the XPS finding reported by both Yun et al. and Ding et al., although those two reports come to different conclusions as to how that should be interpreted. As shown by the AFM measurements, the PEDOT domains increase post laser treatment, lending weight to the agglomeration mechanism of Ding et al., although a similar finding is not seen in the work of Yun et al. This increased domain size is further supported by the XRD data which shows a small but significant increase in the diffraction peaks associated with PEDOT lamella and π - π stacking.

The behaviour of PEDOT:PSS films with different drying conditions provides further insight into the mechanism at play. As is widely reported, films dried at higher temperature and for longer times have a lower native sheet resistance, due to reduced water content meaning the PEDOT cores are closer together. However, upon laser treatment, the increase in conductivity is markedly subdued compared to that of the lower temperature curing, therefore higher water content, films. Indeed, these high temperature films show a minimum sheet resistance almost three times that of the low temperature films (1.1 ± 0.1 k Ω/\square compared to 369 ± 2 Ω/\square). This suggests that the presence of water in the film is crucial to the action of the laser on it, most likely by facilitating the movement and agglomeration of the PEDOT cores, which is not possible when the film is more thoroughly dried. It was also suggested by Ding et al. that the local heating of the film acted to reduce the residual water content, however, based on the thermal modelling, which indicates a very short-lived local heating of around just 50°C, this is unlikely to be a factor in our materials. Were it the case that PSS fragmentation was the primary cause of the conductivity changes, the lack of water in the film would not be expected to have any impact, and the high temperature films would be expected to show changes comparable to the low temperature films. Furthermore, if the change in conductivity was controlled only by the behaviour of the material at the surface, with the PEDOT cores absorbing the laser light and thermally disrupting the PSS shells, it would be expected that the effect would be independent of the film thickness. However, it is clearly seen in figure 3i that the optimal power is highly dependent on the film thickness, indicating that the mechanism responsible for the change in conductivity acts throughout the bulk of the film, not just at the surface.

Taken as a whole, these measurements strongly suggest that

agglomeration of the PEDOT cores is the dominant mechanism in this conductivity control, facilitated by the presence of residual moisture in the films, and occurring throughout the whole thickness of the film.

In order to confirm this, the use of conductive AFM (CAFM) was considered. It was hoped that CAFM would give a direct image of the increase in conductivity of the film, and it was expected that this would highlight the increased PEDOT core sizes. However, CAFM requires the use of a conductive substrate to act as the counter electrode to the AFM tip. Given the sensitivity of this process to the absorption of the laser light, highlighted by the film thickness dependence discussed in section 3.8, changing the substrate is not straight forward. Commonly used doped silicon is unsuitable due to its strong absorption at the laser wavelength which dramatically changes the laser process. Glass coated with indium tin oxide (ITO), was considered as an alternative with much more closely matched optical properties. However, it was found that the laser treatment significantly disrupted the ITO layer in addition to its effects on the PEDOT:PSS, as can be seen in figure S10[†]. Given these challenges, CAFM was considered to be impractical for this work despite its promise.

4 Organic Electrochemical Transistor

To show the utility of this laser based conductivity control, organic electrochemical transistors (OECTs) were demonstrated. The fabrication of these is based on a simple two step process without the need for any photolithographic steps thanks to the use of the laser writing system. In brief, planar OECTs³⁹, with channel and gate in the same single PEDOT:PSS layer, were fabricated from spin coated PEDOT:PSS by first laser ablating unwanted material to define the device footprint, followed by laser irradiating the remaining material to control conductivity. An image of one such device can be seen in figure 4b.

Figures 4c I-III show the output curves for devices fabricated with unirradiated and optimally irradiated PEDOT:PSS, and PEDOT:PSS with addition of ethylene glycol (EG, as conductivity enhancer) and dodecylbenzene sulfonic acid (DBSA, as surfactant needed due to the use of EG).⁹ It can be seen that the maximum transconductance for laser-treated PEDOT:PSS is in line with that of the PEDOT:PSS with additives, with values of 0.147 mS and 0.158 mS respectively.

One significant limitation to the use of PEDOT:PSS as received from the manufacturer in applications such as OECTs is the tendency for the film to delaminate and fragment when exposed to aqueous media. A common approach to preventing this is the addition of a small amount of the cross-linker (3-glycidyloxypropyl)trimethoxysilane (GOPS) to the PEDOT:PSS solution prior to fabrication.⁵⁹ GOPS acts to cross-link the PSS chains, preventing fragmentation, as well as linking the PSS chains with the substrate to prevent delamination. A disadvantage of this is an associated reduction in conductivity of the films, with conductivity shown to fall by up to 99% on addition of 1 v/v% GOPS to pristine PH1000 PEDOT:PSS.⁵⁹

In order to achieve PEDOT:PSS films stable in aqueous media, and therefore suitable for creating stable OECTs, the addition of 0.1 v/v% is sufficient, although this is still reported to cause up

to a 90% drop in conductivity for PH1000 PEDOT:PSS without additional chemical dopants.

Before fabricating OECTs with the addition of GOPS, the effect of the addition of 0.1 v/v% on conductivity was investigated for both laser-treated and additive-treated films. Figure 4a shows that the addition of GOPS did cause an increase in the sheet resistance of untreated PEDOT:PSS, but that the laser-treated material still reached a minimum sheet resistance of 470 Ω/\square , in line with laser-treated material without GOPS.

Figure, 4c IV-VI also show output curves for PEDOT:PSS based OECTs fabricated with 0.1 v/v% GOPS in the unirradiated, irradiated, and additive forms. It can be seen that the laser-treated devices reach similar transconductance values with the addition of GOPS as without, whereas the additive-treated device showed a small reduction in transconductance. It is clear that both the laser and the additive treatments have significant impact on the behaviour of the OECT devices, owing to the massive increase in film conductivity.

5 Conclusion

This work has shown that the conductivity of PEDOT:PSS can be controlled through a laser micro-annealing process, without the use of additives or further post-deposition treatments, from an as-deposited conductivity of $1.1 \pm 0.1 \text{ S cm}^{-1}$ up to $360 \pm 11 \text{ S cm}^{-1}$.

Extensive materials measurements support the proposal that the dominant cause of the changing conductivity is the agglomeration of PEDOT cores within the film, increasing conduction path length before hopping is required. While the work here does not definitively disprove any disruption of the surface PSS layer, neither does it offer a great deal of support in favour of this proposed mechanism. While XPS and work function measurements do indicate that more PEDOT is seen at the surface, this may be caused simply by the growth of the PEDOT cores, pushing out of the plane.

Additionally, the suggestion that this is complemented by the local removal of water is refuted, although it is shown that some residual water is necessary to facilitate the migration of the PEDOT cores.

In combination with laser ablation, simple planar OECTs were fabricated, demonstrating performances similar to devices incorporating the commonly used additives of EG and DBSA. Furthermore, it is shown that this laser process is unaffected by the addition of a small quantity of the cross-linker GOPS, which stabilises PEDOT:PSS films in water, achieving the same high conductivity and OECT transconductance after optimal laser treatment, in contrast to the degraded performance of the films with additives. This photolithography and additive free process paves the way for rapid, low cost device manufacturing in a range of organic bio- and opto-electronic applications.

6 Materials and Methods

6.1 Preparation of PEDOT:PSS films

The PEDOT:PSS films used were spin coated on glass slides from an aqueous solution (Clevios PH1000, Heraeus). Prior to spin coating, the glass slides were cleaned with acetone, isopropyl alcohol, and deionised

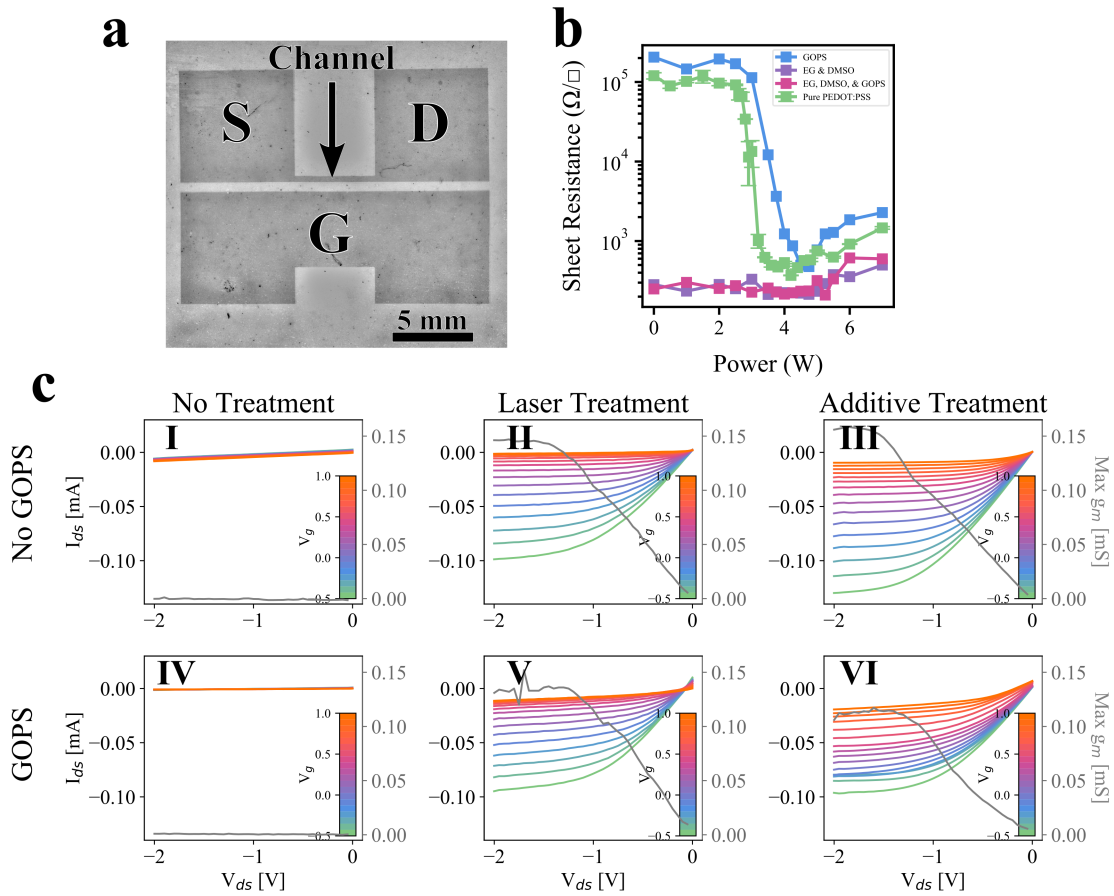


Fig. 4 a) Optical image of the planar OECT devices used, the source (S), drain (D), gate (G) and channel of the device are labelled. b) Sheet resistance of PEDOT:PSS with 0.1 v/v% GOPS after varying the power of the laser treatment, alongside sheet resistance for additive-treated PEDOT:PSS with and without the addition of GOPS. The scale bar is 500 μm . c) Output IV curves for OECTs made with and without the addition of GOPS, using untreated, laser-treated, and additive-treated PEDOT:PSS. The maximum transconductance for each device is shown in grey. Transfer characteristics for the same devices can be found in figure S11[†].

waster (DIW) before receiving a dehydration bake at 120°C for 10 minutes. Finally, the slides received a surface plasma activation with an O₂ plasma for 2 minutes (PlasmaEtch 100, RF power 150 W, O₂ gas flow 50 sccm). The PEDOT:PSS was dispensed through a 0.8 μm syringe filter and spin coated at 1500 rpm for 30 seconds and cured at 120°C for 15 minutes unless otherwise noted. Additive-treated PEDOT:PSS, used for comparison, was made by adding 5 v/v% ethylene glycol (Sigma Aldrich) and 0.1% dodecylbenzene sulfonic acid (Sigma Aldrich), and mixing with magnetic stirrer for 60 minutes, before use to achieve a homogenous dispersion.

6.2 Laser micro-annealing of PEDOT:PSS films

Laser micro-annealing was performed using a pulsed 1064 nm Nd:YAG laser in a laser writing system (LPKF ProtoLaser S). The LPKF laser system comprises the laser, along with focusing optics and mirrors which are used to raster the laser beam across the sample following a CAD design, and an XYZ table to position the sample. The laser beam was defocused from the 25 μm beam waist position to give a spot size diameter of around 400 μm (see figure S11[†]) following the discussion in section 2.1. In this work, the laser frequency was fixed at 15 kHz, while the effect of the other controllable parameters are discussed in section 2. For fabrication of the OECT devices, optimised laser parameters were used to control the conductivity of the PEDOT:PSS, these are summarised in table 3.

Table 3 Parameters used in the LPKF laser writing system for laser micro-annealing and laser ablation.

	Laser Micro-Annealing	Laser Ablation
Power (W)	4.2	4.2
Frequency (kHz)	15	15
Raster Speed (mm/s)	200	300
Line Spacing (μm)	200	50
Laser Spot Diameter (μm)	400	25
Nominal Power Density (W/mm^2)	33	8550

6.3 Laser ablation of PEDOT:PSS films

Laser ablation of PEDOT:PSS has been well studied in the past^{60–62} and the optimisation of this is not discussed here. For the fabrication of OECT devices, laser ablation was performed in the same laser system as the micro-annealing, with the sample placed at the beam waist. To ensure the stability of the laser power the same power was used for both the micro-annealing and ablation steps, although the power density at the PEDOT:PSS is considerably higher for ablation due to the confined beam. The laser parameters for ablation are summarised in table 3. With these parameters there is no visible evidence of PEDOT:PSS remaining, and separate structures are electrically isolated.

6.4 Characterization of PEDOT:PSS films

Film thickness and roughness were characterised by contact and optical profilometry respectively. Contact profiles were recorded across a step from the glass substrate to the film using a Dektak XT-S. 2.5×2.5 mm optical profiles were recorded on a Veeco NT 1100 system, and the data analysed with the Gwyddion software,⁶³ extracting a representative 2D line profile perpendicular to the direction of the laser beam and using a cut-off frequency of 0.05 to separate waviness and roughness parameters. The arithmetic sum of the waviness and roughness is used as the error bars in plotted thicknesses of figure 3a.

Sheet resistance was measured in a van der Pauw setup with a Keithley 2600 source-measure unit (SMU) in ambient conditions. It should be noted that, in situations where anisotropic conductivity is seen, as in figure 2b, measurements based on the van der Pauw method become inaccurate as a prerequisite of the method is that the samples be isotropically conducting. On this basis, where anisotropy is found, the difference between the two orthogonal measurements should be seen as an indication solely of the anisotropy and not as a true measure of the sheet resistance in each direction.

Absorption measurements were performed with a UV-Vis spectrophotometer (UV-2600, Shimadzu) between 200 nm and 1400 nm with 1 nm step size and an accumulation time of 0.1 s. For these measurements, 1 mm thick quartz slides (UQG Optics) were used as the substrate since standard borosilicate glass shows strong absorption below 300 nm (see figure S12[†]).

Work function was measured relative to a gold standard in a KP Technology APS 02 system with a backing voltage of 0.7 V and probe frequency of 72 Hz. Each point was taken as the average of 50 measurements, and the sample value reported as the average over 100 points across a 4×4 μm grid.

AFM images were taken with a Bruker CP-2 system in tapping mode.

XRD patterns were recorded using a XPert PRO MRD using the Cu $K\alpha_1$ line in grazing incidence mode. The incident angle was 0.2° . Measurement step size of 0.12° and a dwell time of 150 seconds were used to record the pattern in the range $2^\circ < 2\theta < 60^\circ$

SEM images were captured with a Carl Zeiss Ultra 55 SEM at an acceleration voltage of 5 keV.

XPS surface chemical state measurements were carried out on a Scienta-Omicron ESCA2SR system using a monochromatic Al $K\alpha$ x-ray source (1486.6 eV). The x-ray source was operated at 100W. The binding energy scale was corrected using the adventitious carbon (284.8 eV). No charging neutraliser was used during the measurements. The data analysis was performed using CasaXPS software. S 2p spectra were fitted with Shirley-type background and mixed Gaussian-Lorentzian functions GL (30) for PSS and asymmetric Lorentzian functions LA(1.05,10,40) for PEDOT. Also, the area ratio and binding energy distance constraints between the spin-orbit splitting (S $2p_{3/2}$ and S $2p_{1/2}$), 2:1 and 1.16 eV, respectively, were taken into account. The quantitative analyses was performed using the elemental sensitivity factors provided by the manufacturer.

Optical images were captured with Nikon SMZ1500 and LV150 optical microscopes.

Electrochemical impedance spectroscopy measurements were performed on a Parastat 4000 potentiometer, using a Pt counter electrode and an Ag/AgCl reference electrode, with the PEDOT:PSS film as the working electrode. A 10 mM KCl solution was used as the electrolyte; an excitation voltage of 10 mV RMS and 0 V DC offset was applied. Measurements were performed between 5 MHz and 10 mHz in a logarithmic step scheme with 10 steps/decade. Finally, data were fitted using a custom written python script with the equivalent circuit shown in the inset of figure 3j.

6.5 Thermal Modelling

A thermal model of the laser interaction of the laser with the PEDOT:PSS was rendered using COMSOL Multiphysics 5.5 using the heat transfer module. The laser was modelled as a 400 μm wide Gaussian beam with laser properties matching those of the real system (15 kHz pulse frequency, 10% duty cycle, 200 mm/s lateral velocity). The outcome of the modelling was found to be independent of duty cycle between 20% and 70% (the range used by the LPKF system to regulate power), provided to average power was kept constant. The absorption of the film was taken from the UV-Vis measurements presented in figure 3d, while thermal conductivity, heat capacity, and density were taken from other works.⁶⁴ The glass carrier slide was modelled using the built-in parameters for glass.

6.6 OECT Fabrication and Measurement

Planar OECT devices were fabricated using PEDOT:PSS films described above with a spin coating speed of 1500 rpm. The footprint of the device was defined by laser ablation using the parameters in table 3, followed by laser micro-annealing across the remaining material. For films incorporating GOPS, the GOPS was added and stirred with a magnetic stirrer for 1 hour immediately before deposition.

7×7 mm device pads were used for all devices, and two gate pads were used to ensure even voltage distribution across the gate. The device width was 5 mm, the separation between channel and gate was 0.5 mm, and the channel and gate lengths were 0.5 mm and 5 mm respectively to match the reported optimal planar OECT geometry of 1:10 ratio between channel and gate area.³⁹

Electrical measurements were made using a Keithley 2600 SMU controlled from a python script and electrical connection was made with pogo pins onto the large PEDOT:PSS pads. A 0.1 ml drop of phosphate-buffered saline solution was placed over the channel and gate, held in place with a PDMS well. The source-drain voltage (V_{ds}) was swept between -2 V and 0 V in 0.05 V steps, and the gate voltage (V_g) was swept from -0.5 V to +1.0 V in 0.1 V steps. At every V_{ds} and V_g set point the current through the source-drain, and through the gate (I_{ds} and I_g respectively) was recorded.

Author Contributions

J.T. conceived the project. J.T. and M.R. designed the experiments. N.P. performed XRD measurements and analysis. J.R.-P., D.P., and J.M. performed XPS measurements and analysis. J.T. performed all other measurements, data analysis and presentation, and wrote the manuscript. T.D. and M.R. supervised the work and provided financial support. All authors discussed the work and reviewed the manuscript.

Conflicts of interest

There are no conflicts to declare.

Acknowledgments

We thank the ID-Fab platform at the Centre Microélectronique de Provence for their support in preparing the samples used in this work. XPS analyses were carried out with the support of CEMNAT and CEITEC Nano Research Infrastructures (projects LM2018103 and LM 2018110) funded by the Ministry of Education, Youth and Sports of the Czech Republic.

Notes and references

- 1 J. Rivnay, S. Inal, B. A. Collins, M. Sessolo, E. Stavrinidou, X. Strakosas, C. Tassone, D. M. DeLongchamp and G. G. Malliaras, *Nature Communications*, 2016, **7**, 11287.
- 2 L. Hu, J. Song, X. Yin, Z. Su and Z. Li, *Polymer*, 2020, **12**, 1–19.
- 3 S. Ho, S. Liu, Y. Chen and F. So, *Journal of Photonics for Energy*, 2015, **5**, 057611.
- 4 J. Rivnay, S. Inal, A. Salleo, R. M. Owens, M. Berggren and G. G. Malliaras, *Nature Reviews Materials*, 2018, **3**, year.

- 5 C. Boehler, Z. Aqrave and M. Asplund, *Bioelectronics in Medicine*, 2019, **2**, 89–99.
- 6 C. M. Proctor, I. Uguz, A. Slezia, V. Curto, S. Inal, A. Williamson and G. G. Malliaras, *Advanced Biosystems*, 2019, **3**, 1–6.
- 7 M. J. Donahue, A. Sanchez-Sanchez, S. Inal, J. Qu, R. M. Owens, D. Mecerreyes, G. G. Malliaras and D. C. Martin, *Materials Science and Engineering R: Reports*, 2020, **140**, 100546.
- 8 M. J. Donahue, C. M. Proctor and X. Strakosas, *Redox Polymers for Energy and Nanomedicine*, Royal Society of Chemistry, 2021, ch. 13, pp. 488–545.
- 9 G. Dijk, A. L. Rutz and G. G. Malliaras, *Advanced Materials Technologies*, 2020, **5**, year.
- 10 Y. Tuchman, T. N. Mangoma, P. Gkoupidenis, Y. Van De Burgt, R. A. John, N. Mathews, S. E. Shaheen, R. Daly, G. G. Malliaras and A. Salleo, *MRS Bulletin*, 2020, **45**, 619–630.
- 11 Y. Van De Burgt and P. Gkoupidenis, *MRS Bulletin*, 2020, **45**, 631–640.
- 12 G. Dijk, A. Kaszas, J. Pas and R. P. O'Connor, *Microsystems & Nanoengineering*, 2022, **8**, year.
- 13 *Journal of Visualized Experiments*, 2022.
- 14 U. Lang, E. Müller, N. Naujoks and J. Dual, *Advanced Functional Materials*, 2009, **19**, 1215–1220.
- 15 J. Ouyang, C.-W. Chu, F.-C. Chen, Q. Xu and Y. Yang, *Advanced Functional Materials*, 2005, **15**, 203–208.
- 16 T. Takano, H. Masunaga, A. Fujiwara, H. Okuzaki and T. Sasaki, *Macromolecules*, 2012, **45**, 3859–3865.
- 17 J. H. Lee, Y. R. Jeong, G. Lee, S. W. Jin, Y. H. Lee, S. Y. Hong, H. Park, J. W. Kim, S. S. Lee and J. S. Ha, *ACS Applied Materials and Interfaces*, 2018, **10**, 28027–28035.
- 18 J. Y. Kim, J. H. Jung, D. E. Lee and J. Joo, *Synthet*, 2002, **126**, 311–316.
- 19 M. Döbbelin, R. Marcilla, M. Salsamendi, C. Pozo-Gonzalo, P. M. Carrasco, J. A. Pomposo and D. Mecerreyes, *Chemistry of Materials*, 2007, **19**, 2147–2149.
- 20 Y. Wang, C. Zhu, R. Pfattner, H. Yan, L. Jin, S. Chen, F. Molina-Lopez, F. Lissel, J. Liu, N. I. Rabiah, Z. Chen, J. W. Chung, C. Linder, M. F. Toney, B. Murmann and Z. Bao, *Science Advances*, 2017, **3**, e1602076.
- 21 Y. Xia and J. Ouyang, *Organic Electronics*, 2010, **11**, 1129–1135.
- 22 N. Kim, B. H. Lee, D. Choi, G. Kim, H. Kim, J. R. Kim, J. Lee, Y. H. Kahng and K. Lee, *Physical Review Letters*, 2012, **109**, 1–5.
- 23 J. Gasiorowski, R. Menon, K. Hingerl, M. Dachev and N. Serdar, *Thin Solid Films*, 2013.
- 24 W. H. Chen, L. Qiu, P. Zhang, P. C. Jiang, P. Du, L. Song, J. Xiong and F. Ko, *Journal of Materials Chemistry C*, 2019, **7**, 10247–10256.
- 25 J. Ouyang, Q. Xu, C.-W. Chu, Y. Yang, G. Li and J. Shinar, *Polymer*, 2004, **45**, 8443–8450.
- 26 D. Alemu, H.-y. Wei, K.-c. Ho and C.-w. Chu, *Energy & Environmental Science*, 2012, **5**, 9662–9671.
- 27 S. M. Kim, C. H. Kim, Y. Kim, N. Kim, W. J. Lee, E. H. Lee, D. Kim, S. Park, K. Lee, J. Rivnay and M. H. Yoon, *Nature Communications*, 2018, **9**, 3858.
- 28 Y. Xia, K. Sun and J. Ouyang, *Advanced Materials*, 2012, **24**, 2436–2440.
- 29 N. Kim, H. Kang, J. H. Lee, S. Kee, S. H. Lee and K. Lee, *Advanced Materials*, 2015, **27**, 2317–2323.
- 30 X. Fan, B. Xu, S. Liu, C. Cui, J. Wang and F. Yan, *ACS Applied Materials and Interfaces*, 2016, **8**, 14029–14036.
- 31 F. Wu, P. Li, K. Sun, Y. Zhou, W. Chen, J. Fu, M. Li, S. Lu, D. Wei, X. Tang, Z. Zang, L. Sun, X. Liu and J. Ouyang, *Advanced Electronic Materials*, 2017, **3**, 1700047.
- 32 C. Wang, K. Sun, J. Fu, R. Chen, M. Li, Z. Zang, X. Liu, B. Li, H. Gong and J. Ouyang, *Advanced Sustainable Systems*, 2018, **2**, 1800085.
- 33 L. Zhang, K. Yang, R. Chen, Y. Zhou, S. Chen, Y. Zheng, M. Li, C. Xu, X. Tang, Z. Zang and K. Sun, *Advanced Electronic Materials*, 2020, **6**, 1900648.
- 34 C. Yun, J. W. Han, S. Kim, D. C. Lim, H. Jung, S. H. Lee, J. W. Jang, S. Yoo, K. Leo and Y. H. Kim, *Materials Horizons*, 2019, **6**, 2143–2151.
- 35 J. Troughton, B. Marchiori, R. Delattre, S. Escoubas, M. Aliouat, S. Grigorian and M. Ramuz, *Organic Electronics*, 2021, **92**, 106108.
- 36 K. Lasisi, W. Yao, T. Ajibade, H. Tian, F. Fang and K. Zhang, *Membranes*, 2020, **10**, 375.
- 37 T. Pflug, A. Anand, S. Busse, M. Olbrich, U. S. Schubert, H. Hoppe and A. Horn, *ACS Applied Electronic Materials*, 2021, **3**, 2825–2831.
- 38 C. F. Ding, Y. T. Lan, H. T. Young and W. T. Hsiao, *Synthetic Metals*, 2021, **275**, 116743.
- 39 M. Ramuz, K. Margita, A. Hama, P. Leleux, J. Rivnay, I. Bazin and R. M. Owens, *ChemPhysChem*, 2015, **16**, 1210–1216.
- 40 A. Nardes, M. Kemerink, M. de Kok, E. Vinken, K. Maturova and R. Janssen, *Organic Electronics*, 2008, **9**, 727–734.
- 41 T. W. Lee and Y. Chung, *Advanced Functional Materials*, 2008, **18**, 2246–2252.
- 42 Y. Xia, K. Sun and J. Ouyang, *Advanced Materials*, 2012, **24**, 2436–2440.
- 43 Y. Xia, K. Sun and J. Ouyang, *Energy & Environmental Science*, 2012, **5**, 5325–5332.
- 44 Y. H. Kim, C. Sachse, M. L. MacHala, C. May, L. Müller-Meskamp and K. Leo, *Advanced Functional Materials*, 2011, **21**, 1076–1081.
- 45 J. Luo, D. Billep, T. Waechter, T. Otto, M. Toader, O. Gordan, E. Sheremet, J. Martin, M. Hietschold, D. R. Zahn and T. Gessner, *Journal of Materials Chemistry A*, 2013, **1**, 7576–7583.
- 46 N. Massonnet, A. Carella, O. Jaudouin, P. Rannou, G. Laval, C. Celle and J.-P. Simonato, *J. Mater. Chem. C*, 2014, **2**, 1278–1283.
- 47 L. Stepien, A. Roch, S. Schlaier, I. Dani, A. Kiriy, F. Simon, M. v. Lukowicz and C. Leyens, *Energy Harvesting and Systems*, 2016, **3**, 101–111.
- 48 I. Zozoulenko, A. Singh, S. K. Singh, V. Gueskine, X. Crispin and M. Berggren, *ACS Applied Polymer Materials*, 2019, **1**, 83–94.
- 49 T. Liu, F. Jiang, J. Tong, F. Qin, W. Meng, Y. Jiang, Z. Li and Y. Zhou, *Journal of Materials Chemistry A*, 2016, **4**, 4305–4311.
- 50 T. A. Yemata, Y. Zheng, A. K. K. Kyaw, X. Wang, J. Song, W. S. Chin and J. Xu, *RSC Advances*, 2020, **10**, 1786–1792.
- 51 E. Jin Bae, Y. Hun Kang, K. S. Jang and S. Yun Cho, *Scientific Reports*, 2016, **6**, 1–10.
- 52 H. Lee, Y. Kim, H. Cho, J. G. Lee and J. H. Kim, *RSC Advances*, 2019, **9**, 17318–17324.
- 53 N. Kim, S. Kee, S. H. Lee, B. H. Lee, Y. H. Kahng, Y. R. Jo, B. J. Kim and K. Lee, *Advanced Materials*, 2014, **26**, 2268–2272.
- 54 E. Hosseini, V. Ozhukil Kollath and K. Karan, *Journal of Materials Chemistry C*, 2020, **8**, 3982–3990.
- 55 H. J. Oh, J. G. Jang, J. G. Kim, J. I. Hong, J. Kim, J. Kwak, S. H. Kim and S. Shin, *Scientific Reports*, 2017, **7**, 1–9.
- 56 S. Eric, B. Christopher, V. Keith, P. Jyoti, K. Rajeev, G. Bobby and I. Ilia, *ACS Applied Materials & Interfaces*, 2017, 1–13.
- 57 D. C. Grahame, *Journal of The Electrochemical Society*, 1952, **99**, 370C.
- 58 D. Harrington, *Journal of the American Chemical Society*, 2002, **124**, 1554–1555.
- 59 A. Håkansson, S. Han, S. Wang, J. Lu, S. Braun, M. Fahlman, M. Berggren, X. Crispin and S. Fabiano, *Journal of Polymer Science, Part B: Polymer Physics*, 2017, **55**, 814–820.
- 60 M. Schaefer, J. Holtkamp and A. Gillner, *Synthetic Metals*, 2011, **161**, 1051–1057.
- 61 D. Karnakis, T. Stephens and G. Chabrol, *Synthetic Metals*, 2013, p. 860711.
- 62 S.-F. Tseng, W.-T. Hsiao, K.-C. Huang and D. Chiang, *Applied Physics A*, 2013, **112**, 41–47.
- 63 D. Nečas and P. Klapetek, *Open Physics*, 2012, **10**, 181–188.
- 64 J. Liu, X. Wang, D. Li, N. E. Coates, R. A. Segalman and D. G. Cahill, *Macromolecules*, 2015, **48**, 585–591.